PHYSICAL REVIEW A **81**, 063623 (2010)

Spin textures in condensates with large dipole moments

J. A. M. Huhtamäki,[1,2] M. Takahashi,[1] T. P. Simula,[1,3] T. Mizushima,[1] and K. Machida[1]
[1]*Department of Physics, Okayama University, Okayama 700-8530, Japan*
[2]*Department of Applied Physics/COMP, Aalto University School of Science and Technology,*
Post Office Box 15100, FI-00076 AALTO, Finland
[3]*School of Physics, Monash University, Victoria 3800, Australia*
(Received 26 March 2010; published 14 June 2010)

We have solved numerically the ground states of a Bose-Einstein condensate in the presence of dipolar interparticle forces using a semiclassical approach. Our motivation is to model, in particular, the spontaneous spin textures emerging in quantum gases with large dipole moments, such as ^{52}Cr or Dy condensates, or ultracold gases consisting of polar molecules. For a pancake-shaped harmonic (optical) potential, we present the ground-state phase diagram spanned by the strength of the nonlinear coupling and dipolar interactions. In an elongated harmonic potential, we observe a helical spin texture. The textures calculated according to the semiclassical model in the absence of external polarizing fields are predominantly analogous to previously reported results for a ferromagnetic $F = 1$ spinor Bose-Einstein condensate, suggesting that the spin textures arising from the dipolar forces are largely independent of the value of the quantum number F or the origin of the dipolar interactions.

DOI: 10.1103/PhysRevA.81.063623 PACS number(s): 03.75.Hh, 03.75.Mn, 75.10.Hk

I. INTRODUCTION

Long-range interparticle forces in a quantum system with a large coherence length is an intriguing combination bound to exhibit a host of fascinating phenomena. Perhaps the most timely example of such a system is the gaseous atomic Bose-Einstein condensate (BEC) subject to magnetic dipole-dipole forces [1].

The dipolar interaction potential, decreasing as r^{-3} in terms of the interparticle distance r, dominates on length scales determined by the coherence length. Other two-body interactions present in the system, such as induced dipolar forces (van der Waals), weaken typically much faster (r^{-6}) and become negligible already over distances of an average interparticle separation. A further interesting aspect of the dipole-dipole interaction is its anisotropy enriching the already diverse finite-size effects in trapped ultracold atomic gases. The magnetic dipolar interaction in condensates has been predicted to give rise to phenomena ranging from spin textures and spontaneous mass currents [2–4] to a roton minimum in the excitation spectrum [5,6], linking the field into the study of liquid He II.

The realization of ^{52}Cr condensates has provided a means of probing dipolar effects experimentally due to the exceptionally large magnetic moments of the atoms [7]. The ground states of a chromium condensate have been studied extensively [8–12]. Anisotropic deformation of an expanding chromium condensate due to dipolar forces has been observed [13], and dipole-induced spin relaxation in an initially polarized ^{52}Cr has been linked to the famous Einstein-de Haas effect in ferromagnets [9,14]. Also, collapse and subsequent d-wave symmetric explosion of dipolar condensates have been recently studied in the case of ^{52}Cr both experimentally and theoretically [15]. Chromium condensates have been recently produced through optical methods [16].

The strength of the magnetic dipolar interaction is determined by the atomic magnetic moment μ_M through the coupling constant $g_d' = \mu_0\mu_M^2/4\pi$, where μ_0 is the permeability of the vacuum. For example, for alkali-metal condensates with total angular momentum quantum number $F = 1$, the magnetic moment is given by $\mu_M = \mu_B g_F$, where μ_B is the Bohr magneton and $g_F = 1/2$ the Landé g factor. Such systems are subject to weak dipolar interactions, e.g., $g_d'/g' \sim 10^{-3}$ for ^{87}Rb, where $g' = 4\pi\hbar^2\,(a_0 + 2a_2)\,/3m$ is the mean-field density-density coupling constant. Here a_0 and a_2 are the s-wave scattering lengths in the channels with total spin 0 and 2, and m is the atomic mass. Nevertheless, dipolar effects have been predicted to be observable in $F = 1$ alkali-metal BECs even in the presence of a magnetic field [17], which was recently confirmed experimentally based on a time-evolution study of a helical spin texture [18]. It has also been proposed that the spin echo in spinor BECs could be utilized in revealing dipole-dipole interactions [19].

The spontaneous occurrence of novel ground-state spin textures in the absence of external magnetic fields requires typically stronger dipolar interactions, $g_d'/g' \sim 10^{-2}$–10^{-1}. Hence, the ^{52}Cr condensates consisting of particles with magnetic moments of $6\,\mu_B$, as opposed to maximal magnetic moments of $1\,\mu_B$ in alkali-metal gases, seem more favorable for observing such effects. Moreover, the rare-earth-metal element Er, with a magnetic moment of $7\,\mu_B$, has been cooled down to μK temperatures [20]. Also, recent developments in trapping and cooling of Dy with the largest atomic magnetic moment of $10\,\mu_B$ yields a promising candidate for observing the predicted spin textures [21]. Developments in the study of ultracold polar molecules provides a means of investigating dipolar effects with large electric moments [22–24].

The study of alkali-metal condensates based on a quantum-mechanical mean-field treatment predicts spin textures with the smallest possible value for the total angular momentum quantum number with internal degrees of freedom, namely, $F = 1$. It is worthwhile to approach an analogous problem from the other extreme limit by treating the magnetic moments of the gas classically [2,25]. By comparing the results predicted by the two models, one may expect that if the predictions agree, they could be of universal character for all dipolar condensates and independent of the particular value of the quantum number F. In general, the quantum-mechanical order parameter has

$2F+1$ components, and the short-range interaction term contains $F+1$ independent coupling constants. Hence, it would be very cumbersome to treat each value of F separately with the complexity of the problem increasing along with F.

Our semiclassical model is briefly described in Sec. II. The order parameter is written in an alternative form compared to previous studies [2,25] in order to simplify analysis and to increase numerical efficiency. The main results are explained in Sec. III: The ground states of the system in harmonic traps of various geometries are described, and the collapse of the spin vortex state is analyzed briefly. The spin helix state is introduced before concluding remarks of Sec. IV.

II. MODEL

In this section, we construct a phenomenological mean-field model describing a trapped Bose-Einstein condensate with local as well as nonlocal interparticle interactions. The model is equivalent to the semiclassical approach previously studied in [2,25], with the exception that now the order parameter field is written in a Cartesian basis yielding a set of three Gross-Pitaevskii type of equations leading to more efficient numerics.

The local interaction is assumed to be of the standard s-wave form, with the coupling constant $g' = 4\pi\hbar^2 a/m$, where a is the s-wave scattering length. Henceforth, we will refer to its dimensionless form $g = 4\pi Na/a_r$, expressed in natural trapping units: $\hbar\omega_r$ is the unit of energy with ω_r being the radial trapping frequency of the confining harmonic potential, and the radial harmonic oscillator length $a_r = \sqrt{\hbar/m\omega_r}$ is the unit of distance. The number of confined atoms is denoted by N. The nonlocal interaction is the anisotropic dipole-dipole interaction with the dimensionless coupling constant g_d which is quantified in relation to g throughout the article. Regardless of whether the origin of the dipolar interactions is considered to be magnetic or electric, we adopt notation and terminology as if it were of the former. For the trapped system to be stable, we find that for a strong enough contact interaction, the value of g_d should not exceed $\sim g/4$, a value very close to the number calculated in the $F=1$ case [3].

The order parameter is taken to be a three-component real-valued vector $\psi = (\psi_x, \psi_y, \psi_z)$. It is straightforward to show that all line defects in such order-parameter space are topologically unstable, because any closed curve on a sphere can be continuously transformed into a point which corresponds to a spin-polarized state [26]. Nevertheless, the energetically stable states can have nontrivial spin textures.

In the present model, the particle density is assumed to be related to the order parameter through $n(\mathbf{r}) = \sum_k \psi_k^2(\mathbf{r})$ and is normalized to unity, $\int d\mathbf{r} n(\mathbf{r}) = 1$. Let us make the assumption that the system is ferromagnetic, and hence we may require that all spins are pointing into the same direction within a small enough region of space. With this simplification, the magnitude of the magnetization density is related to the particle density through

$$|\mathbf{M}(\mathbf{r})| = \mu_M n(\mathbf{r}) = \mu_M \sum_k \psi_k^2(\mathbf{r}) = \sqrt{\sum_k M_k^2(\mathbf{r})}, \qquad (1)$$

where μ_M is the magnetic moment of a single particle, and M_k are the components of magnetization. By squaring, we obtain $\sum_k M_k^2(\mathbf{r}) = \mu_M^2 \sum_k \psi_k^2(\mathbf{r}) n(\mathbf{r})$, which is satisfied if we define

$$M_k(\mathbf{r}) = \mu_M \psi_k(\mathbf{r})\sqrt{n(\mathbf{r})}, \qquad (2)$$

relating the magnetization density to the order parameter. In the following, we omit writing the constant μ_M explicitly and assume it to be included in the coupling constant g_d.

The energy functional $E_{\text{tot}}[\psi_x, \psi_y, \psi_z]$ can thus be written as

$$E_{\text{tot}} = \int \sum_k \psi_k \hat{h} \psi_k d\mathbf{r} + \frac{g}{2}\int n^2 d\mathbf{r} + \frac{g_d}{2}\iint D(\mathbf{r},\mathbf{r}') d\mathbf{r}\, d\mathbf{r}', \qquad (3)$$

where $\hat{h} = -\frac{1}{2}\nabla^2 + V_{\text{trap}}(\mathbf{r})$ is the single-particle Hamiltonian and $V_{\text{trap}} = \frac{1}{2}(x^2 + y^2 + \lambda^2 z^2)$ is the external trapping potential expressed in natural trapping units. For now we will omit external rotation and mass currents in the system, and hence the kinetic energy is merely due to quantum pressure. The second term in Eq. (3) describes the local mean-field s-wave interaction with the coupling constant g, and the final term the nonlocal dipole-dipole interaction with

$$D(\mathbf{r},\mathbf{r}') = \{\mathbf{M}(\mathbf{r})\cdot\mathbf{M}(\mathbf{r}') - 3[\mathbf{M}(\mathbf{r})\cdot\mathbf{e}_R][\mathbf{M}(\mathbf{r}')\cdot\mathbf{e}_R]\}/R^3, \qquad (4)$$

where $\mathbf{R} = \mathbf{r} - \mathbf{r}'$ is the relative coordinate and $\mathbf{e}_R$ the unit vector along it.

Stationary states of the condensate are obtained by differentiating the energy functional with respect to the components of the order parameter with the particle number constraint taken into account through a Lagrange multiplier μ. Differentiation with respect to ψ_j results in a set of three Gross-Pitaevskii (GP) equations

$$\hat{h}\psi_j + gn\psi_j + \frac{g_d}{2}\left[\frac{\sum_k M_k I_k}{n}\psi_j + \sqrt{n} I_j\right] = \mu\psi_j. \qquad (5)$$

Here the functions I_j are defined by

$$I_j(\mathbf{r}) = \int \left[M_j(\mathbf{r}') - 3e_R^j \sum_l M_l(\mathbf{r}') e_R^l\right] \Bigg/ R^3 d\mathbf{r}', \qquad (6)$$

with e_R^l being the lth component of $\mathbf{e}_R$. These integrals may be further broken into convolutions. By applying the convolution theorem, we obtain

$$I_j(\mathbf{r}) = \mathcal{F}^{-1}\left[\sum_l \mathcal{F}[M_l(\mathbf{r})]\hat{f}_{lj}(\mathbf{k})\right], \qquad (7)$$

where $\mathcal{F}$ stands for Fourier transform and $\hat{f}_{lj}(\mathbf{k}) = -\frac{4\pi}{3}(\delta_{lj} - 3k_l k_j/k^2)$ is the Fourier transform of $f_{lj}(\mathbf{r}) = (\delta_{lj} - 3r_l r_j/r^2)/r^3$. The Fourier transforms are efficiently evaluated by using the fast Fourier transform.

From the general form of the GP equations, Eq. (5), it is possible to conclude that the spin-polarized texture is not a stationary state in a confined three-dimensional system in the absence of external polarizing fields when $g_d \neq 0$. Namely, Eq. (5) is of the form $A_{jk}\psi_k = b_j$, where $b_j = \frac{g_d}{2}\sqrt{n} I_j \neq 0$, in general. In the spin-polarized state, we may choose, say, the z axis along the polarization, whence $\psi_x = \psi_y = 0$, yielding $b_x = b_y = 0$ from the general form above. When $g_d \neq 0$, this can be satisfied in regions of nonvanishing density only if $I_x = I_y = 0$. Hence, the bracketed expression in Eq. (7) must vanish identically. As $\hat{f}_{zx}$ and $\hat{f}_{zy}$ are nonvanishing in any finite volume d^3k, continuity of ψ_z implies $M_z(\mathbf{r}) = 0$, which is a contradiction. Such a conclusion can also be drawn from the quantum-mechanical model by following similar arguments.

Apart from the quantum pressure term in Eq. (3), the spin model described above can be viewed as resulting from a classical energy functional. However, the present model can also be argued from the quantum-mechanical spin-F model constrained within the ferromagnetic manifold [27]. With maximally aligned spins, the order parameter at a fixed point $\mathbf{r}$ is of the form $\psi = \sqrt{n}e^{i\theta}e^{-i\hat{F}_z\alpha/\hbar}e^{-i\hat{F}_y\beta/\hbar}e^{-i\hat{F}_z\gamma/\hbar}|z\rangle = \sqrt{n}e^{i(\theta-F\gamma)}e^{-i\hat{F}_z\alpha/\hbar}e^{-i\hat{F}_y\beta/\hbar}|z\rangle$, where $\hat{F}_\alpha$ are the hyperfine spin operators, and $\hat{F}_z|z\rangle = \hbar F|z\rangle$. The order parameter of the classical spin model is obtained if we neglect the phase factor $e^{i(\theta-F\gamma)}$ and replace the quantum-mechanical rotation operators by the classical equivalents and the eigenstate $|z\rangle$ by the unit vector pointing along the z axis. Such substitution should be valid when quantum fluctuations of the spin operator $\hat{\mathbf{F}}$ become negligible. The relative fluctuations in the state $|z\rangle$ are given by $\langle(\hat{\mathbf{F}} - \hbar F)^2\rangle/\langle\hat{\mathbf{F}}^2\rangle = 1/(F+1)$, which vanish in the limit of large F. Possible mass currents arising from local spin-gauge symmetry are neglected when $e^{i(\theta-F\gamma)}$ is set to unity, and the kinetic energy reduces merely to the quantum pressure term in Eq. (3).

III. RESULTS

We have solved the ground states of the system with various values of the coupling constants g and g_d, and the aspect ratio λ. Special emphasis is given to the pancake- and cigar-shaped systems, for which we choose $\lambda = 10$ and $\lambda = 0.10$–0.50, respectively.

A. Ground states in the pancake-shaped limit

Let us first consider the case of a cylindrically symmetric harmonic trap with strong, $\lambda = 10$, confinement in the axial (z) direction. In the presence of dipolar interactions, $g_d > 0$, the magnetic moments tend to lie predominantly in the plane perpendicular to the axial direction in order for the system to minimize dipolar interaction energy.

For a small enough value of g_d/g, the spin texture has typically the flare structure which has been studied previously using the semiclassical approach as well as the quantum-mechanical mean-field model in the $F = 1$ case [2–4]. Such a state is illustrated in Fig. 1(a) for $g = 100$ and $g_d/g = 0.15$. The arrows denote the local direction of magnetization $\mathbf{M}(\mathbf{r})$, whereas the color refers to the particle density $n(\mathbf{r})$. The repulsive interaction between parallel spins separated by a vector perpendicular to the spin vectors causes the magnetization to deviate from the polarized texture. The structure may also be thought of as resulting from the presence of two spin vortices located at the periphery of the cloud. The spin texture is flarelike also in the x-z plane ($y = 0$) due to finite M_z, which is in accordance with the picture that a single toroidal spin vortex encircles the cloud. In the flare state, the magnetization has even parity.

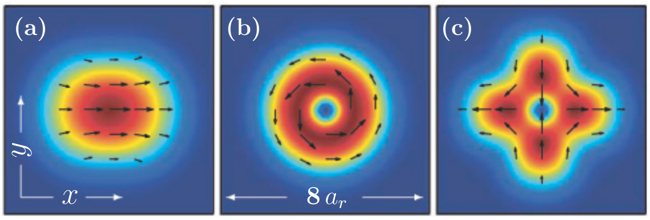

FIG. 1. (Color online) Magnetization $\mathbf{M}(\mathbf{r})$ (arrows) and density $n(\mathbf{r})$ (color) of the (a) flare and (b) spin vortex states for $g = 100$, $g_d/g = 0.15$ in a trap with aspect ratio $\lambda = 10$. Both quantities are shown in the $z = 0$ plane, the density being nearly Gaussian in the axial direction and M_z small. For the chosen parameter values, the flare state in (a) is the energetically favored configuration. Panel (c) illustrates a spin vortex state with opposite spin winding compared to (b). Such a state is not energetically favorable for the parameter values considered in this work. Each panel has dimensions $8\,a_r \times 8\,a_r$.

When the strength of dipolar interactions is increased, the ground state undergoes a second-order phase transition into a state hosting a single spin vortex, which is illustrated in Fig. 1(b) for $g = 100$ and $g_d/g = 0.15$. The density is typically suppressed at the core of the vortex. The spin vortex state has also been studied previously within the semiclassical as well as the $F = 1$ case [2–4]. Analogous to the flare state, the presence of the spin vortex results in a texture which favors dipolar interactions by reducing the repulsive interactions of parallel spins separated by a vector perpendicular to their magnetization. For example, close to the phase transition line in Fig. 2 with $g = 1000$ and $g_d/g = 0.05$, the differences in the kinetic, potential, contact interaction, and dipolar energies of the flare and the spin vortex states are $\Delta E_{\mathrm{kin}} = -0.16$, $\Delta E_{\mathrm{pot}} = 0.077$, $\Delta E_{\mathrm{nl}} = -0.11$, and

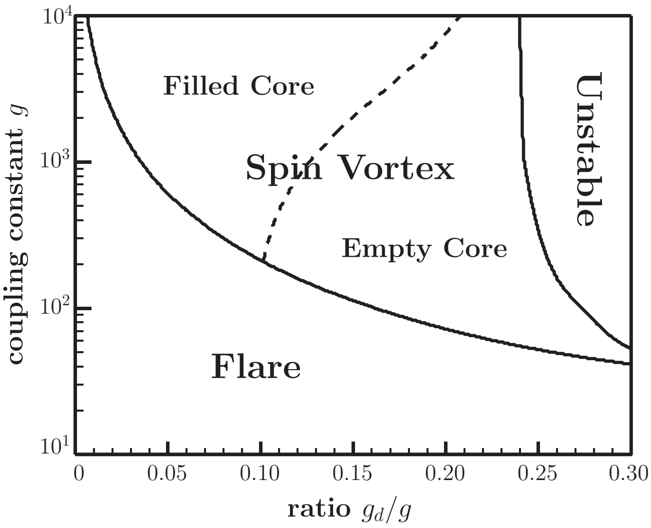

FIG. 2. Ground-state phase diagram of a dipolar condensate in a harmonic trap with aspect ratio $\lambda = 10$. The effective contact interaction coupling constant g is represented in logarithmic scale on the vertical axis. The horizontal axis, measuring the strength of dipolar interactions through the ratio g_d/g, has a linear scale. The phase diagram is divided into three regions: flare [Fig. 1(a)], spin vortex [Fig. 1(b)], and the region where the spin vortex becomes unstable against collapse.

$\Delta E_{\text{dip}} = 0.28$, respectively, leading to a gain in total energy of $\Delta E_{\text{tot}} = 0.077$ in units of $\hbar\omega_r$ per particle.

Figure 1(c) illustrates a spin vortex state with the opposite spin winding. For this texture, the angle between local magnetization and the x axis decreases as the vortex core is circled around in the counterclockwise direction, whereas for the state in Fig. 1(b), the angle increases. Such a state is found only as an excited solution in the present work. In a larger dipolar system, one can construct energetically low-lying spin vortex lattices by arranging the vortices presented in Figs. 1(b) and 1(c), and their negative counterparts ($\mathbf{M} \longrightarrow -\mathbf{M}$) in an alternating square lattice. Both spin vortices presented in Fig. 1 have odd parity.

The ground-state phase diagram in the $(g, g_d/g)$ parameter plane is shown in Fig. 2. The axes of the plane are chosen such that the abscissa is proportional to the particle number N and the ordinate is independent of N and proportional to the (bare) dipolar coupling constant g_d'. The spin vortex state is energetically favored for strong contact and dipolar interactions. The flare state dominates the phase diagram in the limit of weak contact interaction, $g \lesssim 50$, regardless of the strength of dipolar interactions. The phase transition point from flare to spin vortex state depends strongly on the value of g. The spin vortex state becomes unstable toward collapse beyond the critical value of $g_d/g \approx 0.25$ which depends only weakly on the value of g for $g \gtrsim 500$.

With strong enough contact interaction ($g \gtrsim 1000$) and weak dipolar interaction, the cores of the spin vortices are filled with particles whose magnetic moments are pointing in the axial direction. The condensate gains trapping as well as contact interaction energy by filling the vortex core. The dashed line in the phase diagram of Fig. 2 separates the states with filled cores from states with empty cores. On the line $\int n(r=0,z)\,dz / \max \int n(r,z)\,dz = 0.01$ with $r = \sqrt{x^2 + y^2}$, whereas the ratio is close to unity in the upper left corner. The finite axial magnetic moment due to the filled core breaks the inversion symmetry of the state. Instead, the components of $\mathbf{M}$ have the following symmetry: $\hat{P}_z M_{x,y} = -M_{x,y}$, $\hat{P}_z M_z = M_z$, where $\hat{P}_z$ inverts the sign of the x and y coordinates keeping z intact.

For large enough g, the flare state develops continuously into a state with two spin vortices which have ferromagnetic cores as the strength of dipolar interactions is increased. The magnetic moments of the cores are pointing either into the same or opposite directions, the two states being nearly degenerate irrespective of the relative orientation. States hosting multiple spin vortices are found to be energetically unfavorable compared to single spin vortex states for the parameter values considered in this work.

The radial size of the spin vortex state diminishes significantly as the strength of dipolar interactions is increased. This suggests that the reason why the system becomes unstable at some critical value of g_d/g could be due to inward collapse of the condensate. Local and global collapse of a dipolar condensate have been recently studied numerically [28].

In order to understand why the spin vortex solution ceases to exist above the critical point, it is instructive to study scaling transformations of the form

$$\hat{T}^{\sigma}(\tau)\psi_k(r,z) = c^{\sigma}(\tau)\psi_k([1+\tau]r, [1+\sigma\tau]z), \qquad (8)$$

where (r,z) are the cylindrical coordinates, τ is the scaling parameter, σ determines the ratio between axial and radial scaling, and $c^{\sigma}(\tau)$ is chosen to ensure particle number conservation.

Close to the critical point of collapse, the spin vortex state in a pancake-shaped trap is the ground state of the system, and hence lies in a minimum of the energy functional. Under transformations of the form given in Eq. (8), the total energy becomes a function of the scaling parameter τ, $E^{\sigma}_{\text{tot}}(\tau) = E_{\text{tot}}[\hat{T}^{\sigma}(\tau)\psi_k(r,z)]$. Deviation from the ground state always leads to an increase in energy, and hence the second derivative of the total energy with respect to any one-parameter transformation must be positive, $\partial^2_{\tau} E^{\sigma}_{\text{tot}}(\tau)|_{\tau=0} > 0$. The existence of a transformation for which this quantity vanishes indicates that the state becomes unstable against such variation.

Figure 3 shows the value of $\min_{\sigma}\{\partial^2_{\tau} E^{\sigma}_{\text{tot}}(\tau)|_{\tau=0}\}$ as a function of $g_d/g \in [0.10, 0.30]$ scaled by the value at $g_d/g = 0.10$. The solid curve is for $g = 10^4$, dashed for $g = 10^3$, and dash-dotted for $g = 10^2$. The curves are extrapolated (dotted lines) using the last few points to obtain an estimate for the critical value for which the minimum in the energy functional vanishes. The critical values are $g_d/g = (0.240, 0.243, 0.274)$, respectively. The inset in Fig. 3 depicts the value of σ for which $\partial^2_{\tau} E^{\sigma}_{\text{tot}}(\tau)|_{\tau=0}$ is minimized for each g_d/g, the horizontal axis being the same as in the main graph. In the vicinity of the critical point for $g \lesssim 10^3$, $\sigma > 0$, showing that the collapsing cloud shrinks both in radial and axial directions.

Based on a spinor $F = 1$ study, a critical value of $g_d/g \approx 0.24$ has been previously reported for the existence of the spin vortex state [3], where the parameters are chosen such

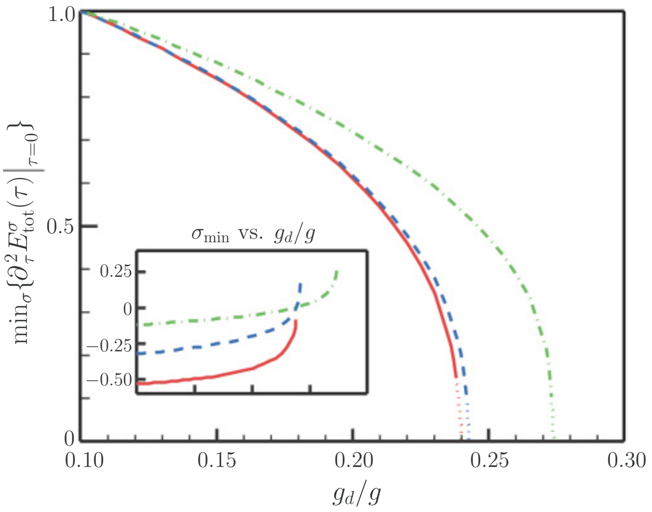

FIG. 3. (Color online) Second derivative of the total energy with respect to a scaling transformation of the form given in Eq. (8) as a function of g_d/g shown in units of the corresponding quantity at $g_d/g = 0.10$. The curves correspond to the parameter values $g = 10^4$ (solid), $g = 10^3$ (dashed), and $g = 10^2$ (dash-dotted). The value of g_d/g for which the second derivative vanishes indicates the critical strength beyond which the spin vortex state becomes unstable against collapse. The inset shows the ratio of axial and radial scaling for which the minimal value of the bracketed expression in the main figure is obtained.

that $g \approx 7000$ in the present study. As the current model is expected to be accurate, apart from possible mass currents, in the limit of large (classical) magnetic moments, this agreement suggests that the critical value for the collapse is universal and independent of F.

B. Ground states in the cigar-shaped limit

Let us now consider solutions to Eq. (5) in an elongated trapping geometry with $\lambda \in [0.10,0.50]$. For definiteness, we will fix $g = 10^4$ which corresponds to a number of $N \approx 1.5 \times 10^5$ ^{87}Rb atoms in a harmonic trap with radial frequency $\omega_r = 2\pi \times 100$ Hz. Regardless of the aspect ratio λ, the solutions are found to exist only within the interval $g_d/g \in [0,0.235]$, agreeing with the result previously reported in the $F = 1$ study [3].

The spins tend to lie predominantly along the axial direction for finite but sufficiently weak dipolar interactions. This ground state resembles the flare state in the pancake-shaped limit, and it has been discussed previously both in $F = 1$ condensates as well as using the semiclassical model [2,4]. Figures 4(a)–4(c) illustrate the spin textures in three radial cross sections of the condensate. Here $\lambda = 0.20$, $g_d/g = 0.030$, and the cross sections are taken at $z = -12\,a_r$,0, and $12\,a_r$, respectively. The color depicts the z component of magnetization, $M_z(\mathbf{r})$, and the color bar is scaled with respect to the maximum magnetization, $\max|\mathbf{M}(\mathbf{r})|$, in the corresponding state. The arrows show the texture projected onto the x-y plane (henceforth referred to as the planar texture), with the length of the arrows scaled within each panel separately, except in Fig. 4(b), for which $M_x = M_y = 0$ by symmetry. The stability range of the flare state depends strongly on the aspect ratio: For example, with $\lambda = 0.50$, the flare state is the ground state for $0 < g_d/g \lesssim 0.01$, with $\lambda = 0.20$ for $0 < g_d/g \lesssim 0.08$, whereas with $\lambda = 0.10$ the flare state dominates the entire stability window.

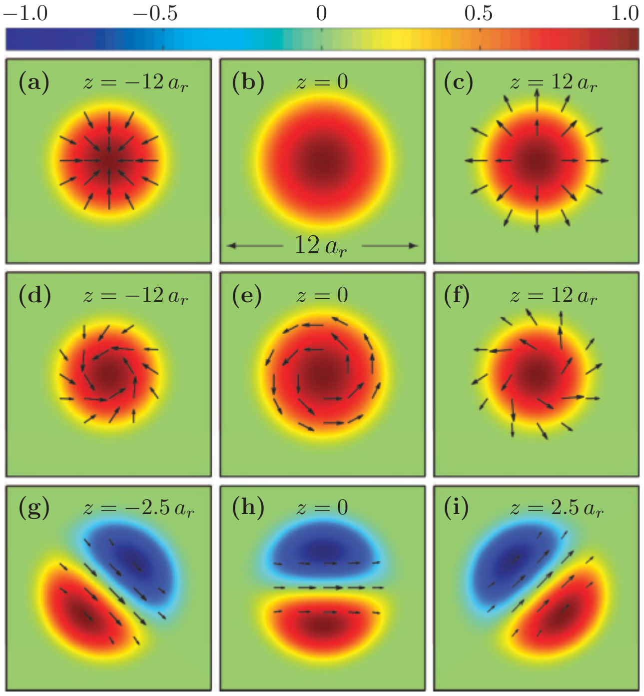

FIG. 4. (Color online) Spin textures in the flare (a)–(c), spin vortex (d)–(f), and spin helix (g)–(i) states in a cigar-shaped trapping geometry with aspect ratio $\lambda = 0.20$ and dipolar interaction strengths $g_d/g = 0.030$, 0.080, and 0.030, respectively. The arrows illustrate the magnetization within a given radial cross section projected onto the x-y plane, whereas the color refers to the axial magnetization M_z normalized with respect to maximal magnetization within each state separately. Each panel has dimensions $12\,a_r \times 12\,a_r$.

Typically, for stronger dipolar interactions, a spin vortex texture appears in the central region of the condensate, illustrated in Figs. 4(d)–4(f) for $\lambda = 0.20$ and $g_d/g = 0.080$. As shown in Fig. 4(e), the planar texture near the center resembles the spin vortex texture in the pancake-shaped geometry discussed before, see Fig. 1(b). As one moves farther away from the center, the planar texture deforms continuously toward the flare texture discussed in the previous paragraph, as depicted in Figs. 4(d) and 4(f). Although the magnetization in both the flare and the spin vortex states has the same symmetry, $\hat{P}_z M_{x,y} = -M_{x,y}$ and $\hat{P}_z M_z = M_z$, the phase transition is sharp, as illustrated below in Fig. 5(d).

In order to characterize the spin vortex state more precisely, we define the following quantities: The axial *column density* reads

$$n_z(z) = \int n(\mathbf{r})dx\,dy. \tag{9}$$

This measures the number of atoms per unit length in the axial direction and is normalized to unity. The average *twisting angle* is given by

$$\alpha(z) = \left\langle \arccos\left[\frac{\hat{\mathbf{r}}_{xy} \cdot \mathbf{M}_{xy}(\mathbf{r})}{M_{xy}(\mathbf{r})}\right]\right\rangle, \tag{10}$$

where $\hat{\mathbf{r}}_{xy} = (x\mathbf{e}_x + y\mathbf{e}_y)/\sqrt{x^2+y^2}$ and the averaging is taken over vectors $\mathbf{M}_{xy}$ whose length exceeds 1% of the maximum of the planar magnetization $M_{xy} = \sqrt{M_x^2 + M_y^2}$. This quantity characterizes the twisting of the magnetization in the plane, yielding zero (or π) for the flarelike textures, Figs. 4(a)–4(c), and $\pi/2$ for the spin vortex texture, Fig. 4(e). The average twisting angle is essentially independent of the radial distribution of the density. Finally, we define the average *tilting angle* through

$$\beta(z) = \left\langle \arctan\left[\frac{M_{xy}(\mathbf{r})}{M_z(\mathbf{r})}\right]\right\rangle, \tag{11}$$

where the averaging is evaluated as above. The tilting angle is related to the pitch of the helical streamlines obtained by following the local direction of magnetization in the spin vortex state, cf. Ref. [3].

Figure 5(a) shows the twisting $\alpha(z)$ in the flare (solid) and spin vortex state (dashed and dash-dotted) for the dipolar interaction strengths $g_d/g = (0.075,0.15,0.235)$, respectively. The flare state is chosen from the neighborhood of the transition point to a spin vortex state. However, $\alpha(z)$ remains nearly zero (or π) over the whole length of the cloud. Small deviation from zero shows that the flare state has even parity only approximately. As the dipolar interaction strength is increased, a spin vortex enters the system. Hence, the twisting angle decreases continuously from π to 0 along the length of the condensate. A plateau of $\alpha(z) \approx \pi/2$ forms in the

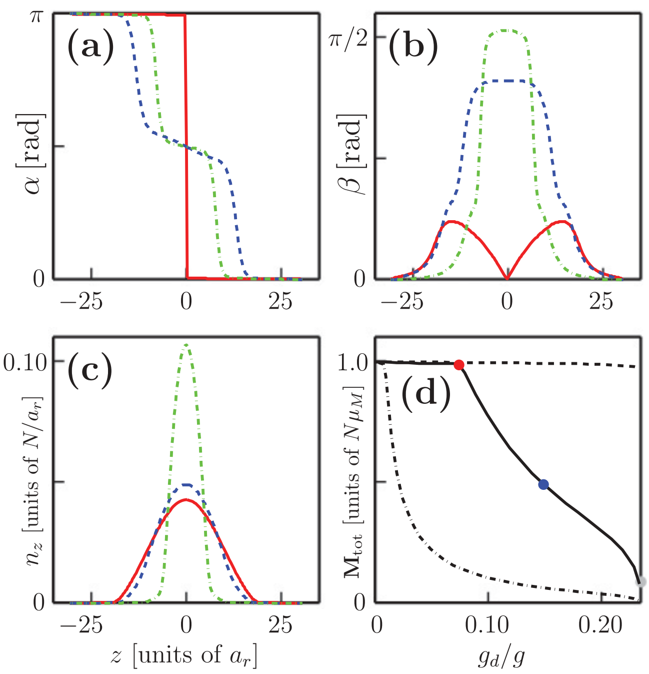

FIG. 5. (Color online) The twisting angle $\alpha(z)$ (a), tilting angle $\beta(z)$ (b), and the axial column density $n_z(z)$ (c) for three values of the dipolar interaction strength $g_d/g = (0.075, 0.15, 0.235)$ shown with solid, dashed, and dash-dotted lines, respectively. The total magnetization $\mathbf{M}_{\rm tot}$, which is directed along the z axis by symmetry, is shown in (d) for the aspect ratios $\lambda = 0.10$ (dashed), 0.20 (solid), and 0.50 (dash-dotted). The dots in (d) refer to the values of g_d/g used in (a), (b), and (c). Units are shown in brackets.

central region of the system for strong dipolar interactions, $g_d/g \gtrsim 0.15$. The width of the plateau decreases for increasing g_d/g due to shrinking of the cloud.

The tilting angle $\beta(z)$ is shown in Fig. 5(b) for the same parameter values as in Fig. 5(a). It remains relatively small in the flare state and experiences a sudden increase at the center of the system when the ground state hosts a spin vortex. For very strong dipolar interactions, $\beta(z) \approx \pi/2$ in the central region, slightly even exceeding $\pi/2$ due to interaction with the axial magnetization of the core region. The small lobes in $\beta(z)$ close to the top and bottom of the cloud are remainders of the flare state.

The strength of dipolar interactions affects the spatial density profile of the spin vortex state significantly. The axial column density $n_z(z)$ is shown in Fig. 5(c) for the parameter values used in 5(a) and 5(b). Not only does the system shrink in the radial but also in the axial direction with increasing g_d/g. Also, the column density appears to be slightly bimodal for strong enough dipolar interactions: The column density is enhanced in the central region of the condensate where the spin vortex lies in order for the system to gain dipolar energy. The width of the plateau in Fig. 5(a) due to the presence of the spin vortex matches the size of the central profile in the bimodal density distribution. The bimodality appears more vividly in elongated systems with $\lambda < 0.20$. In the extreme limit of $g_d/g = 0.235$, the density $n(\mathbf{r})$ in the spin vortex state is significantly reduced close to the center of the trap where $\mathbf{r} \approx 0$.

Figure 5(d) depicts the total magnetization $\mathbf{M}_{\rm tot} = \int \mathbf{M}(\mathbf{r})\,d\mathbf{r}$ in the flare and spin vortex states as a function of g_d/g. Due to symmetry, the total magnetization is along the axial direction. The dashed, solid, and dash-dotted lines correspond to the aspect ratios $\lambda = (0.10, 0.20, 0.50)$, respectively. The sudden drops in total magnetization indicate the phase boundary between the flare and spin vortex states. Whereas the flare state dominates the entire stability window for very elongated trapping geometry ($\lambda = 0.10$), the ground state in a prolate system ($\lambda = 0.50$) hosts a spin vortex already with $g_d/g = 0.01$. The phase transition points for different values of λ agree qualitatively with the analogous results in the $F = 1$ study [3].

It is reasonable to expect that there exist also stationary states with the opposite symmetry compared to the flare and spin vortex states, i.e., $\hat{P}_z M_{x,y}(\mathbf{r}) = M_{x,y}(\mathbf{r})$ and $\hat{P}_z M_z(\mathbf{r}) = -M_z(\mathbf{r})$. There indeed exist low-energy solutions to Eq. (5) with such symmetry, to which we refer to as spin helices. The spin helix state is found, e.g., with $\lambda = (0.10, 0.20, 0.50)$ in the entire stability interval $0 < g_d/g \leqslant 0.235$ of the system. This state resembles closely the state studied in Ref. [18], where the helical spin texture is created by using a transient magnetic field gradient. According to our simulations, the stationary spin helix state exists also in a ferromagnetic $F = 1$ system with dipolar interactions, which will be studied in more detail elsewhere. Dynamical instability of a similar structure in the absence of dipolar interactions has been studied recently [29].

The spin helix texture is illustrated for $\lambda = 0.20$ and $g_d/g = 0.030$ in Figs. 4(g)–4(i), where the radial cross sections are taken at $z = (-2.5\,a_r, 0, 2.5\,a_r)$, respectively. On the z axis, the magnetization lies in the x-y plane, as a consequence of the antisymmetry of M_z. Farther away from the z axis and perpendicular to the magnetization on the axis, M_z becomes the dominant component. The whole planar texture rotates about the z axis as a function of the z coordinate, traversing typically through several cycles along the length of the condensate.

Energetically, the spin helix state appears to be favored by strong dipolar interactions and not too elongated geometries. For example, with $\lambda = 0.50$, the helix becomes energetically favorable compared to the spin vortex state between $0.050 < g_d/g < 0.10$. It is challenging to pinpoint the exact location of the phase transition point due to near degeneracy of the two states. Near the critical value of $g_d/g = 0.235$, the difference in the total energy between the spin vortex and helix states is $\Delta E_{\rm tot} \approx 0.1\hbar\omega_r$ per particle in favor of the helix, which is roughly 2% of the total energy. For $\lambda = 0.20$, the helix state appears to be the minimal energy texture only for $g_d/g \gtrsim 0.20$, whereas for $\lambda = 0.10$, the flare state lies 2%–7% lower in energy over the entire stability range of the system.

The number of cycles in the helix texture increases as the condensate is elongated, and thus for the sake of clarity we illustrate it as an excited state for $\lambda = 0.10$ and $g_d/g = 0.20$ in Figs. 6(a)–6(c). In Fig. 6(a), the solid and dashed curves show the components M_x and M_y along the z axis, respectively, and the M_z component along the y axis is shown in the inset by the dash-dotted curve.

The spin helix can be thought of as two elongated stripes, polarized along the z axis in the opposite directions, intertwined around one another. The helical texture on the z axis arises due to continuous twisting of the magnetization

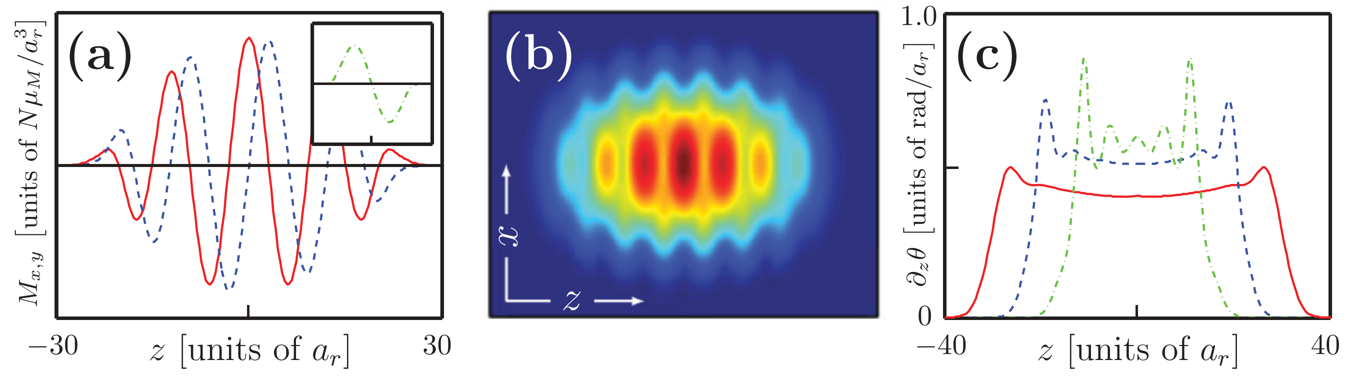

FIG. 6. (Color online) (a) M_x (solid) and M_y (dashed) on the z axis as a function of z in the spin helix state for $\lambda = 0.10$ and $g_d/g = 0.20$. The dash-dotted curve in the inset shows M_z along the y axis in the range $[-5,5]\,a_r$. The vertical axis spans the interval $[-0.0028,0.0028]\,N\mu_M/a_r^3$ both in the main figure and the inset. (b) The column density $n(x,z) = \int n(\mathbf{r})\,dy$ illustrating density oscillations characteristic of the spin helix state for strong dipolar interactions. The parameters are as in (a), and the field of view is $8\,a_r \times 60\,a_r$. (c) Wave vector of the spin helix state for $g_d/g = (0.080,0.20,0.23)$ shown with solid, dashed, and dash-dotted curves, respectively. The peaks at the ends of the cloud are finite-size effects. Units are shown in brackets.

via the x-y plane. In the $F = 1$ case, quantized spin vortices of opposite winding penetrate through the axially polarized ferromagnetic stripes, forming an intertwined spin vortex pair. Intertwining of two mass vortices has been previously studied in relation to the splitting of a doubly quantized vortex in a scalar condensate [30,31].

Figure 6(b) illustrates the column density $n(x,z) = \int n(\mathbf{r})\,dy$ for the same state as in Fig. 6(a), red denoting an area of high and blue of vanishing particle density. With strong dipolar interactions, density oscillation appears spontaneously due to the helix spin texture: for a fixed point in the x-y plane close to the surface region of the cloud, the axial magnetization M_z is an oscillating function of z. The particle density is suppressed in the vicinity of the nodes of M_z and enhanced at the antinodes due to dipolar interactions.

As a measure of the pitch of the spin helix, we define the angle

$$\theta(z) = \arctan\left[\frac{M_y(0,0,z)}{M_x(0,0,z)}\right]. \tag{12}$$

The derivative $\partial\theta/\partial z$ yields the wave vector of the helix, which is plotted in Fig. 6(c) for $\lambda = 0.10$ and $g_d/g = (0.080,0.20,0.23)$ with the solid, dashed, and dash-dotted curves, respectively. The wave vector tends to increase for stronger dipolar interactions, which is reasonable because the dipolar coherence length decreases as $\xi_d \propto g_d^{-1/2}$. The peaks in $\partial\theta/\partial z$ at the top and bottom of the cloud are finite-size effects: The texture may adjust freely into an energetically favorable configuration at the edge as one of the boundary conditions due to continuity of the order parameter is liberated. Oscillations penetrate along the whole length of the condensate for $g_d/g = 0.23$. These oscillations enhance rapidly as the strength of dipolar interactions is increased even further.

The number of cycles in the spin helix state decreases as the aspect ratio $\lambda = \omega_z/\omega_r$ is increased, until in spherical geometry, the direction of the spin on the z axis twists only through half a cycle along the length of the system, cf. Fig. 6(a). Interestingly, the spin vortex state, for which the magnetization has the opposite symmetry with respect to inversion about the z axis, reduces to the spin helix state, rotated by $(\pm)\pi/2$ about $\mathbf{e}_z \times \mathbf{M}_\mathrm{h}$, where $\mathbf{M}_\mathrm{h}$ is the magnetization at the trap center in the helix state.

IV. SUMMARY AND CONCLUSIONS

We have studied spin textures arising from dipolar interactions in gaseous Bose-Einstein condensates of particles with large permanent dipole moments. The theory is based on a semiclassical model treating the dipole moments of the bosons classically.

The observed spin textures in clouds confined in harmonic trapping potentials agree qualitatively with previously reported results for an $F = 1$ system [3,4], such as ^{87}Rb. Moreover, the ground-state phase transition points with respect to the strength of dipolar interactions seem to agree roughly with both weak and tight axial trapping frequency. The qualitative agreement in the observations drawn from the two models suggests that similar textures and phase diagrams are to be expected also for ferromagnetic systems with $F > 1$ and for condensates consisting of electric dipoles.

A major difference between our semiclassical model and the quantum-mechanical model describing a magnetic system lies in the existence of mass currents: In the quantum-mechanical case, phase gradients of the components of the order parameter emerge spontaneously possibly giving rise to mass currents which are absent in the semiclassical treatment, see the last paragraph of Sec. II. The main effect from taking spontaneous mass currents into account regarding the present results would be that the phase transition line between the flare and the spin vortex states in Fig. 2 is shifted to the right due to increased kinetic energy of the spin vortex state. Spin dynamics of ferromagnetic condensates has been studied recently in the long-wavelength limit using a hydrodynamic model [32].

In addition to solving the ground states of the system for various parameter values, we investigate the spin vortex state in the extreme limit of the dipolar interaction strength $g_d/g \approx 1/4$. For larger dipolar interactions, the state becomes unstable against collapse of the cloud due to strong attractive forces overwhelming the quantum pressure term and repulsive interparticle interactions. The estimated point of instability agrees well with the value observed in the $F = 1$ study [3].

In the limit of tight axial confinement, two ground states are observed, namely, the flare and the spin vortex states. For prolate geometries, an additional spin helix texture appears as a low-energy stationary state. The helix is the ground state of the system only in slightly prolate condensates and for strong dipolar interactions. This state is most likely related to the S state reported in [3] and is especially interesting in relation to the experimental observation of dipolar effects in ^{87}Rb utilizing a similar spin texture [18]. The magnetization pattern of the spin helix gives rise to spontaneous density oscillations in the stationary state for strong dipolar interactions. As in the case of the spin vortex and flare textures, the helix state ceases to exist for $g_d/g \gtrsim 1/4$.

ACKNOWLEDGMENTS

The authors would like to thank the Japan Society for the Promotion of Science (JSPS) for financial support. Y. Kawaguchi is acknowledged for useful comments.

---

[1] T. Lahaye, C. Menotti, L. Santos, M. Lewenstein, and T. Pfau, Rep. Prog. Phys. **72**, 126401 (2009).
[2] M. Takahashi, S. Ghosh, T. Mizushima, and K. Machida, Phys. Rev. Lett. **98**, 260403 (2007).
[3] S. Yi and H. Pu, Phys. Rev. Lett. **97**, 020401 (2006).
[4] Y. Kawaguchi, H. Saito, and M. Ueda, Phys. Rev. Lett. **97**, 130404 (2006).
[5] D. H. J. O'Dell, S. Giovanazzi, and G. Kurizki, Phys. Rev. Lett. **90**, 110402 (2003).
[6] L. Santos, G. V. Shlyapnikov, and M. Lewenstein, Phys. Rev. Lett. **90**, 250403 (2003).
[7] A. Griesmaier, J. Werner, S. Hensler, J. Stuhler, and T. Pfau, Phys. Rev. Lett. **94**, 160401 (2005).
[8] K. Góral, K. Rzążewski, and T. Pfau, Phys. Rev. A **61**, 051601(R) (2000).
[9] L. Santos and T. Pfau, Phys. Rev. Lett. **96**, 190404 (2006).
[10] R. B. Diener and T.-L. Ho, Phys. Rev. Lett. **96**, 190405 (2006).
[11] H. Mäkelä and K.-A. Suominen, Phys. Rev. A **75**, 033610 (2007).
[12] L. He and S. Yi, Phys. Rev. A **80**, 033618 (2009).
[13] J. Stuhler, A. Griesmaier, T. Koch, M. Fattori, T. Pfau, S. Giovanazzi, P. Pedri, and L. Santos, Phys. Rev. Lett. **95**, 150406 (2005).
[14] Y. Kawaguchi, H. Saito, and M. Ueda, Phys. Rev. Lett. **96**, 080405 (2006).
[15] T. Lahaye, J. Metz, B. Fröhlich, T. Koch, M. Meister, A. Griesmaier, T. Pfau, H. Saito, Y. Kawaguchi, and M. Ueda, Phys. Rev. Lett. **101**, 080401 (2008).
[16] Q. Beaufils, R. Chicireanu, T. Zanon, B. Laburthe-Tolra, E. Maréchal, L. Vernac, J.-C. Keller, and O. Gorceix, Phys. Rev. A **77**, 061601(R) (2008).
[17] Y. Kawaguchi, H. Saito, and M. Ueda, Phys. Rev. Lett. **98**, 110406 (2007).
[18] M. Vengalattore, S. R. Leslie, J. Guzman, and D. M. Stamper-Kurn, Phys. Rev. Lett. **100**, 170403 (2008).
[19] M. Yasunaga and M. Tsubota, Phys. Rev. Lett. **101**, 220401 (2008).
[20] A. J. Berglund, J. L. Hanssen, and J. J. McClelland, Phys. Rev. Lett. **100**, 113002 (2008).
[21] M. Lu, S. H. Youn, and B. L. Lev, Phys. Rev. Lett. **104**, 063001 (2010).
[22] H. L. Bethlem, G. Berden, and G. Meijer, Phys. Rev. Lett. **83**, 1558 (1999).
[23] M. W. Mancini, G. D. Telles, A. R. L. Caires, V. S. Bagnato, and L. G. Marcassa, Phys. Rev. Lett. **92**, 133203 (2004).
[24] K. Ni, S. Ospelkaus, M. de Miranda, A. Pe'er, B. Neyenhuis, J. Zirbel, S. Kotochigova, P. Julienne, D. Jin, and J. Ye, Science **322**, 231 (2008).
[25] M. Takahashi, S. Ghosh, T. Mizushima, and K. Machida, Eur. Phys. J. B **68**, 391 (2009).
[26] N. D. Mermin, Rev. Mod. Phys. **51**, 591 (1979).
[27] T.-L. Ho and V. B. Shenoy, Phys. Rev. Lett. **77**, 2595 (1996).
[28] N. G. Parker, C. Ticknor, A. M. Martin, and D. H. J. O'Dell, Phys. Rev. A **79**, 013617 (2009).
[29] R. W. Cherng, V. Gritsev, D. M. Stamper-Kurn, and E. Demler, Phys. Rev. Lett. **100**, 180404 (2008).
[30] M. Möttönen, T. Mizushima, T. Isoshima, M. M. Salomaa, and K. Machida, Phys. Rev. A **68**, 023611 (2003).
[31] J. A. M. Huhtamäki, M. Möttönen, T. Isoshima, V. Pietilä, and S. M. M. Virtanen, Phys. Rev. Lett. **97**, 110406 (2006).
[32] A. Lamacraft, Phys. Rev. A **77**, 063622 (2008).